

Research Article

Visible Light-Driven Mn-MoS₂/rGO Composite Photocatalysts for the Photocatalytic Degradation of Rhodamine B

Thi Thuy Trang Phan,¹ Thanh Tam Truong,¹ Ha Tran Huu,¹ Le Tuan Nguyen,¹ Van Thang Nguyen^{1,2}, Hong Lien Nguyen,³ and Vien Vo^{1,2}

¹Faculty of Natural Sciences, Quy Nhon University, Qui Nhon 590000, Vietnam

²Applied Research Institute for Science and Technology, Quy Nhon University, Qui Nhon 590000, Vietnam

³School of Chemical Engineering, Hanoi University of Science and Technology, Hanoi 100000, Vietnam

Correspondence should be addressed to Vien Vo; vovien@qnu.edu.vn

Received 19 June 2020; Accepted 22 July 2020; Published 13 August 2020

Academic Editor: Cláudia G. Silva

Copyright © 2020 Thi Thuy Trang Phan et al. This is an open access article distributed under the Creative Commons Attribution License, which permits unrestricted use, distribution, and reproduction in any medium, provided the original work is properly cited.

The $n\%$ Mn-MoS₂/rGO (labeled as $n\%$ MMS/rGO, where $n\% = \text{Mn}/(\text{Mn} + \text{Mo})$ in mol) composites were successfully prepared by a facile hydrothermal method from the Mn-MoS₂ (MMS) and rGO precursors, in which the MMS was obtained by a facile one-step calcination of (NH₄)₆Mo₇O₂₄·4H₂O, (NH₂)₂CS, and Mn(CH₃COO)₂·4H₂O as precursors in N₂ gas at 650°C. The samples were characterized using X-ray diffraction (XRD), Fourier-transform infrared spectroscopy (FTIR), scanning electron microscopy (SEM), transmission electron microscopy (TEM), electron paramagnetic resonance spectroscopy (EPR), UV-visible diffuse reflectance spectroscopy (UV-Vis DRS), and X-ray photoelectron spectroscopy (XPS), which indicates the composites containing nanosheets of Mn-MoS₂ and rGO components. The photocatalytic activities of the $n\%$ MMS/rGO composite photocatalysts were evaluated through the photodegradation of rhodamine B (RhB) under the visible light irradiation. The enhancement in the photocatalytic performance of the achieved composites was attributed to the synergic effect of Mn doping and rGO matrix. The investigation of photocatalytic mechanism was also conducted.

1. Introduction

Environmental pollution is becoming more serious, leading to a significant negative impact on human health and the ecological environment. Among these challenges, water pollution caused by waste compounds from the discharge of industries such as paper, paint, printing, and textile is concerned as the most serious one [1]. Therefore, the treatment of wastewater for reducing its contamination is one of the urgent issues that attract much attention. There are numerous approaches for eliminating these contaminants, in which the photocatalytic degradation under visible light is the most attractive one [2].

As promising photocatalysts, oxide semiconductors, such as TiO₂ [3], ZnO [4], WO₃ [5], and Ta₂O₅ [6], have been widely investigated. However, their optical absorption in the visible light region is hindered by their broad band gap,

preventing them from employing in the photocatalytic water treatment process. Recently, the two-dimensional (2D) layered transition-metal dichalcogenides have attracted worldwide attention in the solar cell, environmental, hydrogen evolution catalysts, and energy fields [7]. Among them, molybdenum disulfide (MoS₂), a 2D semiconducting material with outstanding electronic and optical properties, is constructed from layers consisting of a plane of Mo atoms sandwiched between two planes of S atoms. Therefore, MoS₂ has tailorable band gap depending on the number of MoS₂ layers (from 1.2 eV in bulk to 1.9 eV in monolayer) [8]. Thanks to its narrow band gap, MoS₂ is capable of strong absorption in the visible light region to create electron-hole pairs, allowing MoS₂ to be a promising visible light-driven photocatalyst for practical applications [9]. However, the most common disadvantage of pure MoS₂ photocatalyst is the rapid recombination of the photo-generated electron-

hole pairs, resulting in low photocatalytic activities [9]. To overcome this problem, combination with other materials and doping strategy are the two most general solutions. The improvement in the photocatalytic activities of the host material via the element doping could be attributed to the enhanced effect in interfacial charge-transfer reactions of dopants [10]. Doping transition metals such as Co, Ni, and Fe into the S-edge of MoS₂ could modify the edge site activity for hydrogen evolution reaction [11]. Graphene, a typical well-known material with 2D structure, is applied in various fields such as fuel cells, supercapacitors, sensors, solar cells, batteries, water treatment, adsorbent, and reinforcement for polymer. Recently, graphene and its derivatives such as graphene oxide (GO) and reduced graphene oxide (rGO) have emerged as a key matrix material for designing photocatalysts, in which they contribute to enhance the conductivity and reduce the recombination of the photo-generated electron-hole pairs [12]. Therefore, an integration of MoS₂ into graphene or its derivatives may lead to a heterostructure with some favorable properties, such as fast electron mobility and increased optical absorbance, facilitating the photocatalytic activities in the visible light region [13].

In this article, to our knowledge, for the first time, photocatalytic degradation of rhodamine B (RhB) on the Mn-MoS₂/rGO composites is reported. A photocatalytic mechanism for the photodegradation of RhB was proposed.

2. Materials and Methods

2.1. Materials. All chemicals, including graphite powder (Merck, Germany, ≥99%), L-ascorbic acid (HiMedia Laboratories Pvt. Ltd., India, ≥99%), ammonium heptamolybdate tetrahydrate (NH₄)₆Mo₇O₂₄·4H₂O, Mn(CH₃COO)₂·4H₂O, and thiourea (NH₂)₂CS (Merck Germany, ≥99%), KMnO₄, NaNO₃, H₂SO₄, HCl, H₂O₂, C₂H₅OH, and rhodamine B (Xilong Chemical Co., Ltd. China, ≥90%), P25 (TiO₂, Sigma-Aldrich, ≥99.5%), were used without further purification.

2.2. Preparation of Samples. GO was prepared from graphite powder using the Hummers method [14]. rGO was synthesized by reducing GO with L-ascorbic acid agent. Mn-MoS₂ was prepared via a facile method of calcinating the mixture of (NH₄)₆Mo₇O₂₄·4H₂O, (NH₂)₂CS, and Mn(CH₃COO)₂·4H₂O as the precursors. In a typical experiment, [NH₄]₆Mo₇O₂₄·4H₂O and (NH₂)₂CS were dissolved in a solvent of water:ethanol (1:1, v/v) under vigorously stirring at room temperature for 30 minutes. A proper amount of Mn(CH₃COO)₂·4H₂O was added and continuously stirred for another 1 h to obtain a homogeneous solution. The resulting solution was heated at 60°C under stirring to evaporate solvents, and then, a solid was obtained. This solid was well ground and calcinated at 650°C for 1 hour in N₂ gas. The obtained samples were labeled as *n* %MMS, where *n*% = Mn/(Mn + Mo) in mol. For comparison, MoS₂ was also prepared in the same procedure without the addition of Mn(CH₃COO)₂·4H₂O and denoted as MS.

The *n*%MMS/rGO composites were fabricated by a facile hydrothermal method from *n*%MMS and rGO. In a typical procedure, 4 mg of *n*%MMS (*n* = 1, 3, 5, and 7) and 1 mg of rGO were dispersed in a solvent of water:ethanol (1:1, v/v) under stirring for 5 hours. This mixture was transferred into 100 mL Teflon-lined autoclave and treated at 180°C for 10 hours. A black precipitate was collected using centrifugation and washed with distilled water and ethanol before being dried at 80°C for 10 hours and labeled as *n*%MMS/rGO (*n* = 1, 3, 5, and 7).

2.3. Characterization of Materials. The powder X-ray diffraction (XRD) patterns were recorded on a D8 Advanced Bruker X-ray diffractometer with Cu-Kα ($\lambda = 1.5406 \text{ \AA}$) radiation. The Fourier-transform infrared spectra were measured at room temperature using an IRPrestige-21 spectrophotometer (Shimadzu). Scanning electron microscopy (SEM) and energy dispersive spectrometry (EDS) were conducted on a SEM-JEOL-JSM 5410 LV (Japan). The high-resolution transmission electron microscopy (HR-TEM) image, selected area electron diffraction (SAED), and fast Fourier transformation (FFT) patterns were obtained with an operating voltage of 200 kV on a JEOL TEM-2100F microscope. The UV-Vis absorption spectra were recorded using a GBC Instrument-2885 spectrophotometer. The X-ray photoelectron spectroscopy (XPS) spectra were measured using a Theta Probe AR-XPS System (Thermo Fisher Scientific). The electron paramagnetic resonance (EPR) spectra were obtained on a Bruker A300 spectrometer at X-band frequency (9.8492 GHz).

2.4. Photocatalytic Activity. Photocatalytic activities were evaluated through the photodegradation of RhB in aqueous solution under the visible light irradiation. For a typical experiment, 0.1 g of the photocatalyst was dispersed into a 400 mL RhB solution with a concentration of 20 mg/L under stirring at room temperature. Before irradiation, the suspension was stirred in the dark for 2 hours to reach the adsorption-desorption equilibrium of RhB molecules on the surface of the photocatalyst before being illuminated by the compact light (60 W-220 V). After every interval of 30 minutes, 4 mL solution was taken out and centrifuged to remove the photocatalyst. The residual concentration of RhB as a function of investigated time was determined by recording its absorbance at 553 nm using a UV-Vis spectrometer. For comparison, photocatalytic activity of P25 was evaluated with the same procedure as mentioned above.

3. Results and Discussion

Crystal structure of MS, MMS (abbreviation for 3%MMS), and *n*%MMS/rGO composites was investigated by XRD, and their patterns are shown in Figure 1(a). As can be seen, the XRD patterns of *n*%MMS/rGO composites, MMS, and MS are analogous with the peaks at $2\theta = 14.1, 33.6, 39.84, 58.1,$ and 68.96° corresponding to (002), (100), (103), (110), and (201) planes of the hexagonal MoS₂ phase, respectively [15].

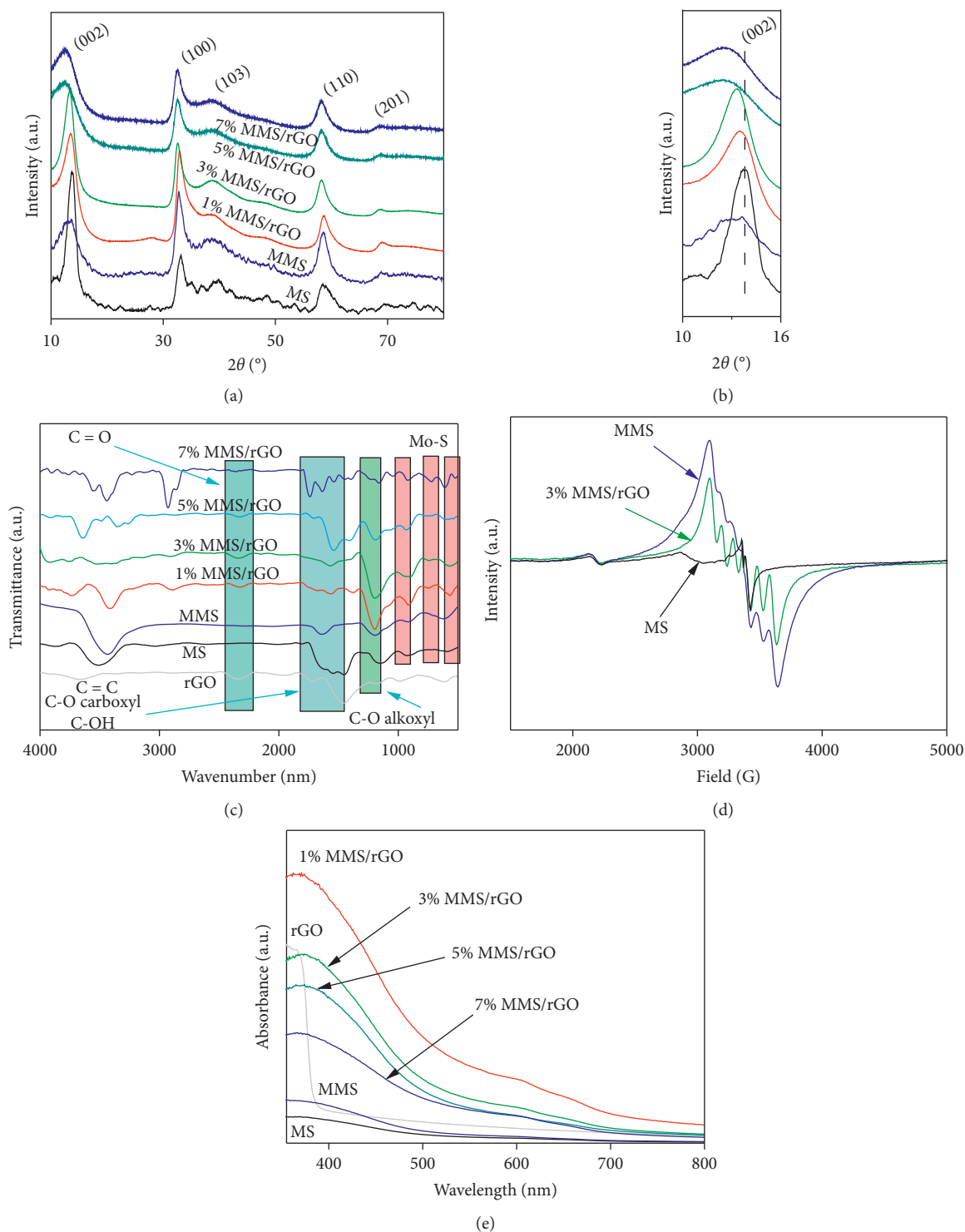


FIGURE 1: (a) XRD patterns; (b) XRD patterns with enlargement of (002) peak; (c) FTIR; (e) UV-Vis spectra of MS, MMS, and $n\%$ MMS/rGO composites; (d) EPR spectra of MS, MMS, and 3%MMS/rGO.

It is worth mentioning here that characteristic diffraction peak due to stacked rGO is absent in $n\%$ MMS/rGO composites, which demonstrates that rGO is not stacked in $n\%$ MMS/rGO [16]. The strong peak at $2\theta = 14.1^\circ$ (002), corresponding to d-spacing of 0.62 nm, elucidates a well-stacked layered structure of MoS₂ in the composites [17]. In

addition, no peaks for MnS or other impurity phases were observed, suggesting that Mn may be successfully doped into the MoS₂ host [18]. Particularly, the peak intensity of the obtained composites decreases for increasing the content of Mn. Furthermore, the enlargement of 2θ range of 10–16° (as shown in Figure 1(b)) shows a slight shift of (002) peak to the

lower-angle region, which indicates the increase in interlayer spacing of the doped samples. This expansion could be explained by the larger ionic radius of Mn^{2+} (0.067 nm) than that of Mo^{4+} (0.065 nm), according to Shannon ionic radius [19] at a coordination number of 6 [20].

Figure 1(c) presents the FTIR spectra of MS, MMS, and $n\%$ MMS/rGO composites. For all the materials, the peaks around 450, 528, and 920 cm^{-1} are corresponding to Mo-S stretching vibrations [16, 21, 22], which demonstrates the presence of MoS_2 in the materials. For rGO, the peaks at 1060, 1619, 1224, and 1720 cm^{-1} are attributed to C-O (alkoxy) stretching vibrations [23], C=C stretches from the unoxidized graphitic domain [24], C-OH stretching [25], and C=O stretching of carboxyl group [25], while the vibration band around 2350 cm^{-1} could be ascribed to C=O stretching of CO_2 from the air. The nature of bonding found by IR spectra could be a further confirmation of the coexistence of MoS_2 and rGO in the achieved composites.

EPR spectroscopy was used to investigate the effect of doping Mn ions on MMS and composite structures. Figure 1(d) shows the room temperature EPR spectra of the MS, MMS, and 3%MMS/rGO. Accordingly, the type of defects presents in the prepared nanoparticles can be studied by the g factor calculated by $g = h\nu/BH_0$ [26]. The low pristine intensity for MS with factor $g = 2.003$ (with magnetic field = 3350 Gauss) is shown in Figure 1(c), which may be due to defects such as vacancy S that serves as the paramagnetic center of the material, while the weak EPR at high field could be assigned for the localized defect related to Mo due to the dislocation and dangling bond [20]. The EPR signals of the doped samples show a hyperfine split into six peaks corresponding to the electron-spin interaction of Mn^{2+} ion with nuclear-spin of $I = 5/2$ [27, 28]. The Mn doping-induced defect could serve as a trapping site to reduce the recombination rate of photo-generated charged carriers, which may enhance photocatalytic activities of the doped samples.

The UV-Vis DRS spectra of rGO, MS, MMS, and $n\%$ MMS/rGO composites are shown in Figure 1(e). The absorption edges of MS, MMS, and $n\%$ MMS/rGO composites extend to 800 nm, suggesting that the absorption of the composites is completely in the visible light region. Compared to the sole MMS, the absorption intensity of $n\%$ MMS/rGO composites is significantly enhanced over the entire investigated range of wavelength, which could be attributed to the intrinsic light absorption of rGO. Therefore, the combination with rGO could enhance the visible light harvesting ability of the obtained composites, which is favorable for improving their photocatalytic performance. In addition, due to high electronic conductivity, rGO could offer a good diffusion pathway for electron to extend the lifetime of electron-hole pairs which finally could overcome the intrinsic limitation of high recombination rate of the single MoS_2 [14].

The surface morphology of the photocatalysts was investigated by SEM and TEM. As observed in Figure 2(a), rGO is constructed from nanosheets with the thickness of ~ 10 nm that is consistent with the TEM image in Figure 2(e)

and confirms the successful exfoliation of rGO via the chemical reduction by *L*-ascorbic acid agent. As shown in Figures 2(b) and 2(c), the surface morphology of MS and MMS is composed of nanosheets aggregated together. There is no significant change in the aggregation of MoS_2 nanosheets in both samples, which may lead to less exposed active sites and inferior activity. Normally, MoS_2 is a *p*-type semiconductor with low conductivity, easy to agglomerate, and poor in charge transfer capacity, which makes the material has low catalytic activity [29]. Therefore, dispersion in a high specific surface area matrix as rGO could be an effective way to not only reduce the agglomeration but also lessen the charge transfer resistance. According to Figure 2(d), the better dispersion could be observed after combining Mn-doped MoS_2 with rGO matrix. This observation is also confirmed by the TEM image in Figure 2(f). Furthermore, the interlayer $d_{(002)}$ -spacing of 0.65 nm, calculated from the line profile (using Image J tools) in HR-TEM image of Figure 2(g), shows a slight expansion compared to the theoretical value [30], which is in good agreement with the aforementioned XRD discussion. The crystal structure of the 3%MMS/rGO composite was further verified by the FFT patterns and the SAED shown in Figures 2(h) and 2(i). The values of the lattice spacing are 2.82 and 1.61 Å, which are corresponding to the (100) and (110) planes of 2H- MoS_2 , respectively [31], which both are confirmed in SAED pattern (Figure 2(i)). The halo ring and unclear dot arrangement in FFT and SAED patterns illustrate for the low crystallinity of the material.

The XPS measurement was performed on a representative material 3%MMS/rGO. The Mn2p XPS spectrum (Figure 3(a)) can be deconvoluted into six peaks corresponding to Mn^{2+} at binding energies of 640 and 651.48 eV, Mn^{3+} at 642.3 and 653.8 eV, and Mn^{4+} at 645 and 654.8 eV [32–34]. This result suggests the coexistence of Mn^{2+} , Mn^{3+} , and Mn^{4+} ions on the surface of the sample. Figure 3(b) presents Mo3d XPS spectrum with two peaks at 229.16 and 232.43 eV corresponding to the $\text{Mo}^{4+}3d_{5/2}$ and $\text{Mo}^{4+}3d_{3/2}$, respectively. In addition, the peak at 226.9 eV is attributed to S2s of MoS_2 [35]. The S2p XPS spectrum in Figure 3(c) contains two peaks at 161.8 and 162.9 eV, which are assigned to the $\text{S}2p_{3/2}$ and $\text{S}2p_{1/2}$ of S^{2-} species in the composite [36]. The C1s XPS spectrum in Figure 3(d) can be split into four peaks, in which peaks at 284.8, 285.7, 287.9, and 288.9 eV are attributed to the C-C/C=C, C-S/C-O, C=O, and O-C=O bonds, respectively, for functional groups in the rGO [37] and from C-S bonds [38].

The photocatalytic activities of MS, MMS, and $n\%$ MMS/rGO were evaluated through the photodegradation of RhB in aqueous solution under the visible light irradiation (Figure 4(a)). It can be observed that, after photodegradation for 240 minutes, the concentration of RhB decreases by about 25.9% in the presence of MS; however, the degradation is significantly enhanced by MMS (41%). This indicates that Mn doping in MoS_2 results in an increase in the photodegradation efficiency of the obtained material. Remarkably, compared to the sole components, the composites show a much higher photodegradation efficiency. Among them, 3% MMS/rGO exhibits the highest photodegradation efficiency

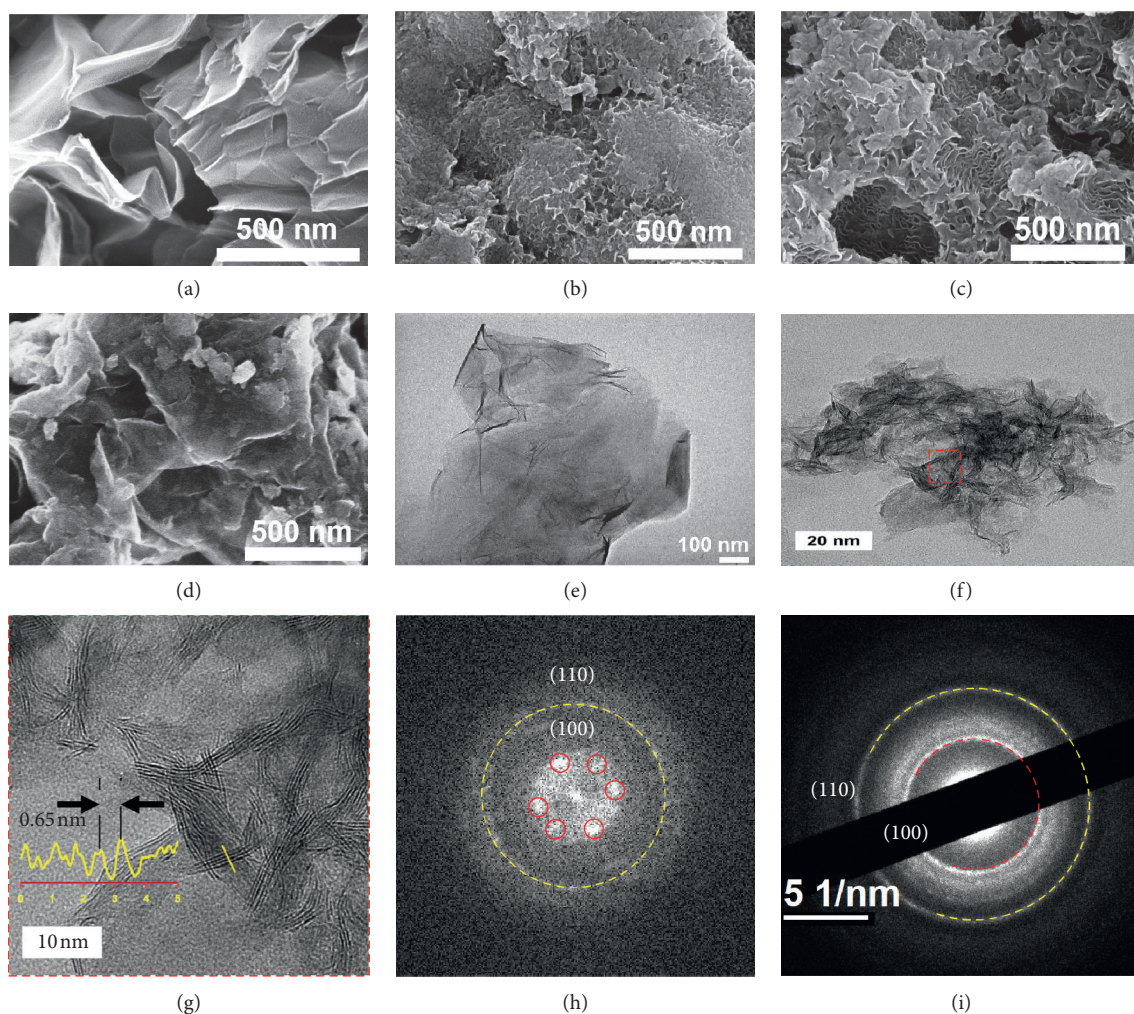


FIGURE 2: SEM images of rGO (a), MS (b), MMS (c), and 3%MMS/rGO (d). TEM images of rGO (e), 3%MMS/rGO (f, g), FFT (h), and SAED (i) of 3%MMS/rGO.

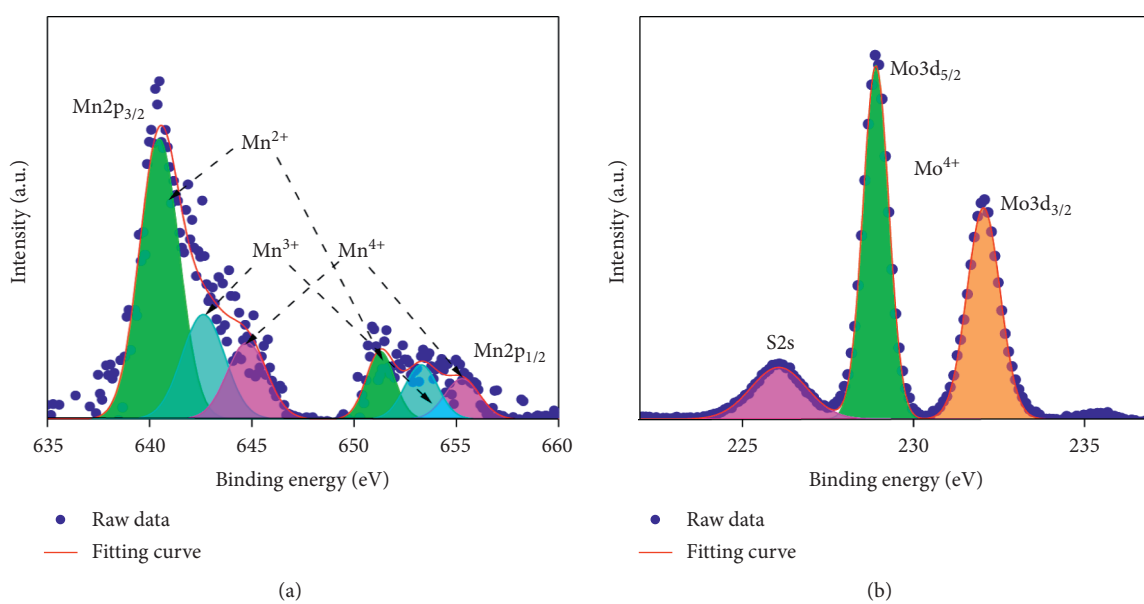


FIGURE 3: Continued.

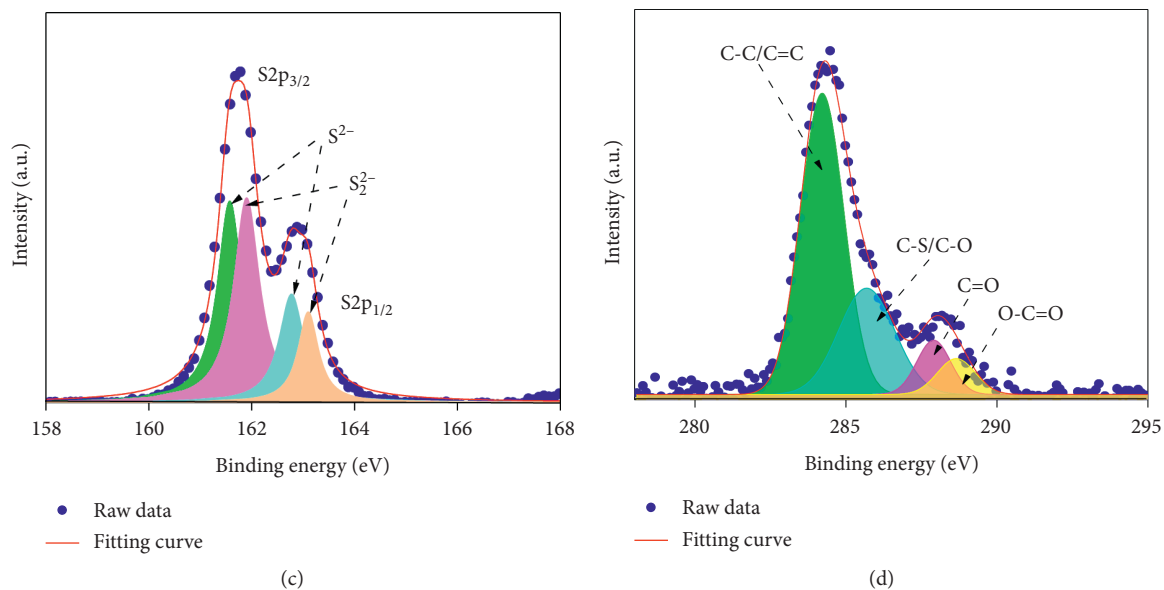


FIGURE 3: XPS spectra of 3%MMS/rGO.

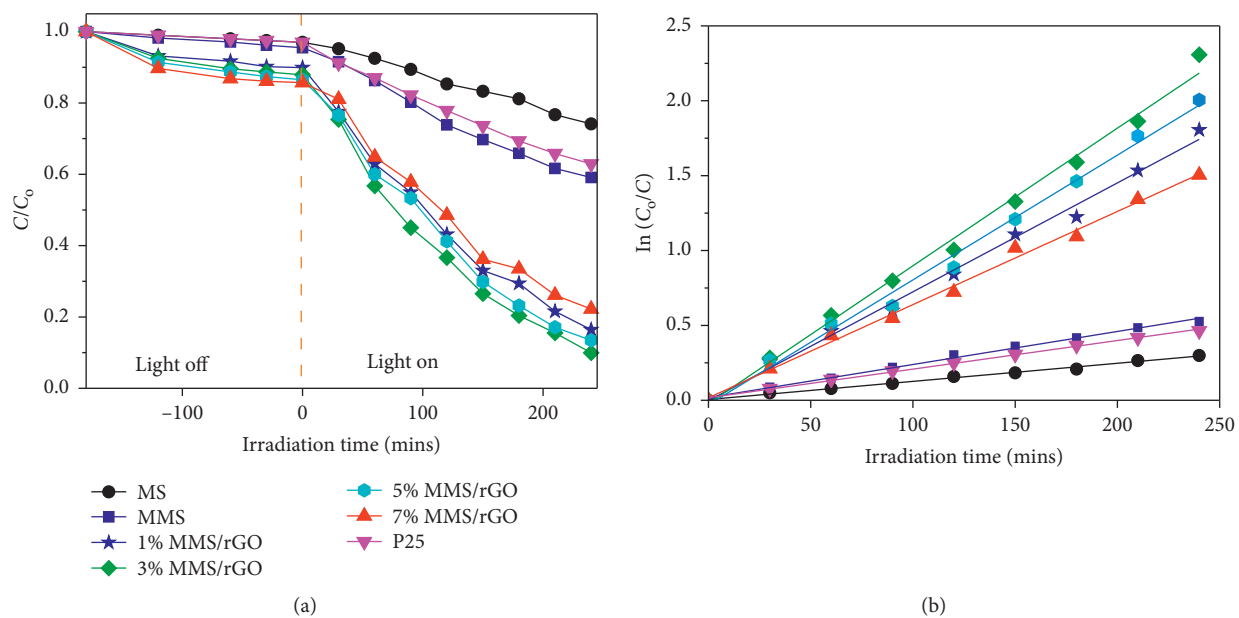


FIGURE 4: Continued.

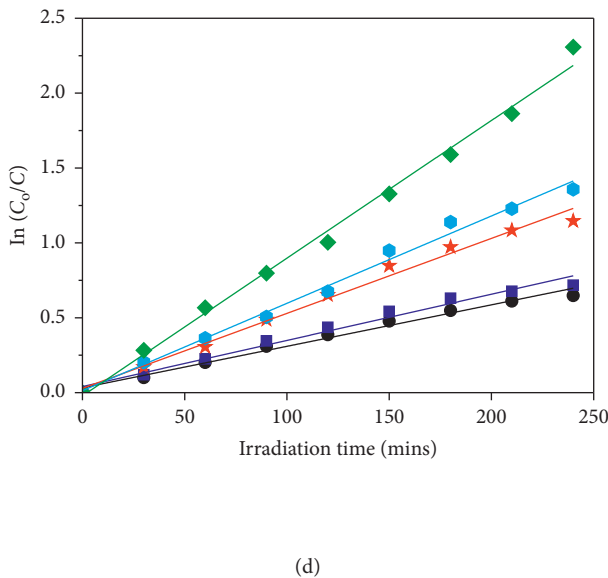
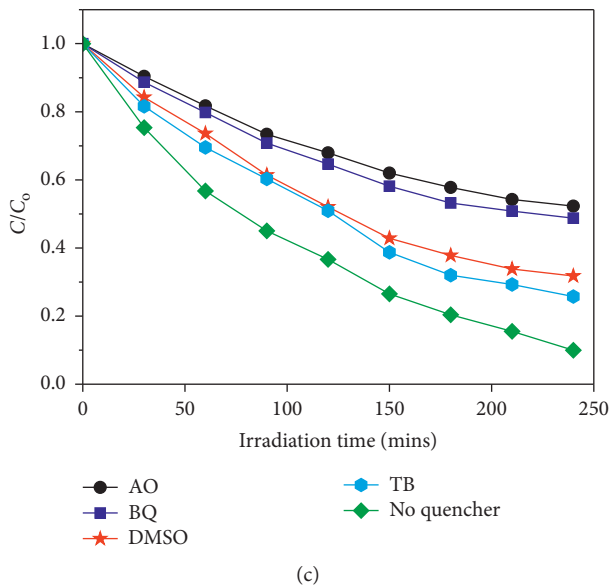


FIGURE 4: (a, b) Photocatalytic activities of P25, MS, MMS, and $n\%$ MMS/rGO composites; (c, d) photocatalytic activities of 3%MMS/rGO with different trapping agents for RhB degradation under visible light irradiation.

of 90%. This suggests that rGO plays a pivotal role in enhancing the photocatalytic performance of the composites. A comparison between the composites shows that the photocatalytic activity increases from $n = 1$ to 3 but decreases when n at higher values of 5 and 7. For comparison with other works, photocatalytic activity of P25 was evaluated with the same procedure, and the result is shown in Figures 4(a) and 4(b). It is observed that the composites show the much better photocatalytic performance with the higher rate constants compared to P25 (the commercial TiO_2). Accordingly, Mn doping in MoS_2 along with combination of rGO is an effective strategy in modification of MoS_2 as a photocatalyst with enhanced catalytic performance.

Normally, in order to evaluate the kinetics of the photocatalytic progress, the Langmuir–Hinshelwood model has been applied [39]. Figure 4(b) shows the linear relationship of $\ln(C_0/C)$ versus the irradiation time, indicating that the photodegradation of RhB fits well with the pseudo-first-order kinetic model according to the equation $\ln(C_0/C) = k \cdot t$, where C is the equilibrium concentration of RhB (mg/L), C_0 is the initial concentration of RhB before irradiation (mg/L), t (min) is the reaction time, and k (min^{-1}) is the reaction rate constant. The obtained data are summarized in Table 1.

Accordingly, the 3%MMS/rGO shows the highest rate constant of 0.00919 min^{-1} , which is 7.6 and 4.16 times higher than MS and MMS, respectively. This may be due to a substantial synergic effect between Mn- MoS_2 and rGO on enhancement in the photocatalytic performance of the composite.

In order to clarify the main active species responsible for the degradation of RhB over 3%MMS/rGO, controlled photocatalytic activity experiments were performed with the addition of different radical scavengers at the natural pH of the dye. In this study, four different scavengers,

TABLE 1: Rate constant of the photocatalytic degradation of RhB on MS, MMS, and $n\%$ MMS/rGO composites.

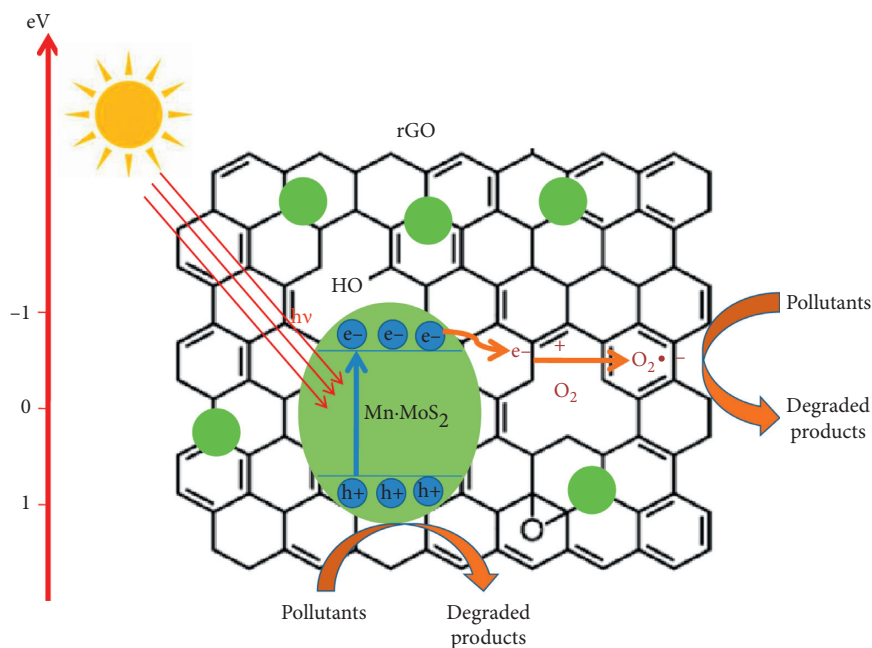
Samples	Rate constant k_{app} (min^{-1})	Correlation coefficients (R^2)
MS	0.00121	0.994
MMS	0.00221	0.994
1%MMS/rGO	0.00727	0.993
3%MMS/rGO	0.00919	0.993
5%MMS/rGO	0.00833	0.993
7%MMS/rGO	0.00622	0.993
P25	0.00191	0.997

tert-butyl alcohol (TB) scavenger for $\cdot\text{OH}$ [40], ammonium oxalate (AO) for H^+ [41], 1,4-benzoquinone (BQ) for O_2^- [42], and dimethyl sulfoxide (DMSO) for e^- [43], were used. Figure 4(c) shows the photocatalytic activities of 3%MMS/rGO for the degradation of RhB in the presence of different radical scavengers. The obtained data are summarized in Table 2.

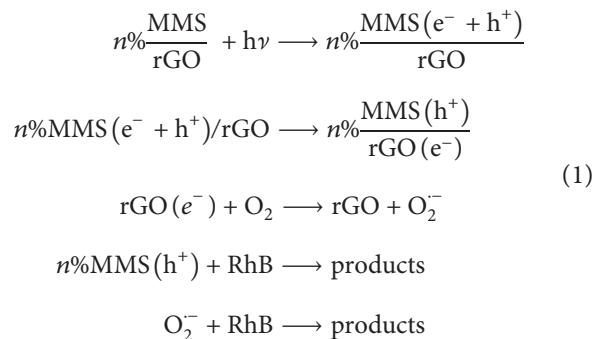
These results indicate that h^+ and O_2^- may play a major role, whereas $\cdot\text{OH}$ and e^- are minor active species in the photodegradation of RhB. Based on the effect of scavengers, a mechanism for the photocatalytic degradation of RhB over $n\%$ MMS/rGO is proposed in Figure 5. Accordingly, when light is absorbed, photoelectrons (e^-) from the conduction band of MoS_2 are transferred to rGO. The photoelectrons will then react with O_2 molecule adsorbed on the photocatalyst surfaces to form O_2^- radicals. These O_2^- radicals and active photoholes (h^+) degrade RhB. In this process, the rGO acts as a sink for

TABLE 2: Rate constant for the photocatalytic degradation of RhB on 3%MMS/rGO with and without the addition of the scavengers.

Samples	Rate constant k_{app} (min^{-1})	Correlation coefficients (R^2)
No scavenger	0.00919	0.993
DMSO	0.00583	0.990
TB	0.00501	0.987
BQ	0.00308	0.978
AO	0.00277	0.983

FIGURE 5: Proposed mechanism for the photocatalytic degradation of RhB over $n\%$ MMS/rGO.

the excited electrons because of its π -conjugation structure. Mn is as acceptors of photoelectrons from MoS_2 , and the transferred process could restrain the recombination of holes and electrons, facilitating the photocatalytic performance. The photocatalytic degradation of RhB on the $n\%$ MMS/rGO composite can be illustrated as follows:



4. Conclusions

$n\%$ MMS/rGO composites containing nanosheets of Mn- MoS_2 and rGO components were successfully fabricated using the hydrothermal method. Among the prepared

composites, 3%MMS/rGO exhibits the highest RhB degradation efficiency (90%) much higher than that of Mn-doped MoS_2 (41%) and MoS_2 (25.9%). The mechanism for the photocatalytic decomposition of RhB on 3%MMS/rGO was proposed, in which photoelectrons (e^-) from the conduction band of MoS_2 transferring to rGO and photoholes (h^+) in the valence band of MoS_2 play a pivotal role in the photo-degradation of RhB. This work can contribute a facile preparation to design a heterostructured photocatalyst with enhanced photocatalytic performance for the practical applications in the field of the wastewater treatment.

Data Availability

The data used to support the findings of this study are available from the corresponding author upon request.

Conflicts of Interest

The authors declare that they have no conflicts of interest.

Acknowledgments

This work was financially supported by the Vietnam Ministry of Science and Technology (Grant no. NĐT.52.KR/19).

References

- [1] A. Agrawal, R. S. Pandey, and B. Sharma, "Water pollution with special reference to pesticide contamination in India," *Journal of Water Resource and Protection*, vol. 2, no. 5, pp. 432–448, 2010.
- [2] R. Ameta, S. Benjamin, A. Ameta et al., "Photocatalytic degradation of organic pollutants: a review," *Materials Science Forum*, vol. 734, pp. 247–272, 2013.
- [3] L. Yu, L. Wang, X. Sun et al., "Enhanced photocatalytic activity of rGO/TiO₂ for the decomposition of formaldehyde under visible light irradiation," *Journal of Environmental Sciences*, vol. 73, pp. 138–146, 2018.
- [4] Z. Kalantari Bolaghi, S. M. Masoudpanah, and M. Hasheminasari, "Photocatalytic activity of ZnO/RGO composite synthesized by one-pot solution combustion method," *Materials Research Bulletin*, vol. 115, pp. 191–195, 2019.
- [5] W. Zhua, F. Suna, R. Goei et al., "Facile fabrication of RGO-WO₃ composites for effective visible light photocatalytic degradation of sulfamethoxazole," *Applied Catalysis B: Environmental*, vol. 207, pp. 93–102, 2017.
- [6] S. Ambreen, M. Danish, N. D. Pandey, and A. Pandey, "Investigation of the photocatalytic efficiency of tantalum alkoxy carboxylate-derived Ta₂O₅ nanoparticles in rhodamine B removal," *Beilstein Journal of Nanotechnology*, vol. 8, pp. 604–613, 2017.
- [7] B. Balasubramaniam, N. Singh, P. Kar et al., "Engineering of transition metal dichalcogenide-based 2D nanomaterials through doping for environmental applications," *Molecular Systems Design & Engineering*, vol. 4, no. 4, pp. 804–827, 2019.
- [8] R. Zhang, W. Wan, D. Li, F. Dong, and Y. Zhou, "Three-dimensional MoS₂/reduced graphene oxide aerogel as a macroscopic visible-light photocatalyst," *Chinese Journal of Catalysis*, vol. 38, no. 2, pp. 313–320, 2017.
- [9] Y. Yuan, P. Shen, Q. Li et al., "Excellent photocatalytic performance of few-layer MoS₂/graphene hybrids," *Journal of Alloys and Compounds*, vol. 700, pp. 12–17, 2017.
- [10] A. Tripathi, M. Mathpal, P. Kumar et al., "Structural, optical and photoconductivity of Sn and Mn doped TiO₂ nanoparticles," *Journal of Alloys and Compounds*, vol. 622, pp. 37–47, 2015.
- [11] H. Wang, C. Tsai, D. Kong et al., "Transition-metal doped edge sites in vertically aligned MoS₂ catalysts for enhanced hydrogen evolution," *Nano Research*, vol. 8, no. 2, pp. 566–575, 2015.
- [12] R. K. Upadhyay, N. Soin, and S. S. Roy, "Role of graphene/metal oxide composites as photocatalysts, adsorbents and disinfectants in water treatment: a review," *RSC Advances*, vol. 4, no. 8, pp. 3823–3851, 2014.
- [13] L. Zhang, L. Sun, S. Liu et al., "Effective charge separation and enhanced photocatalytic activity by the heterointerface in MoS₂/reduced graphene oxide composites," *RSC Advances*, vol. 6, no. 65, pp. 60318–60326, 2016.
- [14] W. S. Hummers Jr. and R. E. Offeman, "Preparation of graphitic oxide," *Journal of the American Chemical Society*, vol. 80, no. 6, p. 1339, 1958.
- [15] J. Prasad, A. K. Singh, K. K. Haldar, V. Gupta, and K. Singh, "Electromagnetic interference shielding effectiveness in 3D flower-like MoS₂-rGO/gadolinium-doped nanocomposites," *Journal of Alloys and Compounds*, vol. 788, pp. 861–872, 2019.
- [16] S. Kumar, V. Sharma, K. Bhattacharyya, and V. Krishnan, "Synergetic effect of MoS₂-RGO doping to enhance the photocatalytic performance of ZnO nanoparticles," *New Journal of Chemistry*, vol. 40, no. 6, pp. 5185–5197, 2016.
- [17] Y. Zhong, T. Shi, Y. Huang et al., "Three-dimensional MoS₂/graphene aerogel as binder-free electrode for li-ion battery," *Nanoscale Research Letters*, vol. 14, no. 85, pp. 1–8, 2019.
- [18] L. Wu, X. Xu, Y. Zhao et al., "Mn doped MoS₂/reduced graphene oxide hybrid for enhanced hydrogen evolution," *Applied Surface Science*, vol. 425, pp. 470–477, 2017.
- [19] R. D. Shannon, "Revised effective ionic radii and systematic studies of interatomic distances in halides and chalcogenides," *Acta Crystallographica Section A*, vol. 32, no. 5, pp. 751–767, 1976.
- [20] J. Wang, F. Sun, S. Yang et al., "Robust ferromagnetism in Mn-doped MoS₂ nanostructures," *Applied Physics Letters*, vol. 109, no. 9, Article ID 092401, 2016.
- [21] A. S. Krishna Kumar, S.-J. Jiang, and J. K. Warchol, "Synthesis and characterization of two-dimensional transition metal dichalcogenide magnetic MoS₂@Fe₃O₄ nanoparticles for adsorption of Cr(VI)/Cr(III)," *ACS Omega*, vol. 2, no. 9, pp. 6187–6200, 2017.
- [22] J. Liu, Y. Li, J. Ke, Z. Wang, and H. Xiao, "Synergically improving light harvesting and charge transportation of TiO₂ nanobelts by deposition of MoS₂ for enhanced photocatalytic removal of Cr(VI)," *Catalysts*, vol. 7, no. 30, 2017.
- [23] X.-L. Yin, L.-L. Li, D.-C. Li, and J.-M. Dou, "One-pot synthesis of CdS-MoS₂/RGO-E nano-heterostructure with well-defined interfaces for efficient photocatalytic H₂ evolution," *International Journal of Hydrogen Energy*, vol. 43, no. 45, pp. 20382–20391, 2018.
- [24] H.-L. Guo, X.-F. Wang, Q.-Y. Qian, F.-B. Wang, and X.-H. Xia, "A green approach to the synthesis of graphene nanosheets," *ACS Nano*, vol. 3, no. 9, pp. 2653–2659, 2009.
- [25] C. Xu, R.-s. Yuan, and X. Wang, "Selective reduction of graphene oxide," *New Carbon Materials*, vol. 29, no. 1, pp. 61–66, 2014.
- [26] L.-T. Tseng, X. Luo, T. Tan, S. Li, and J. Yi, "Doping concentration dependence of microstructure and magnetic behaviours in Co-doped TiO₂ nanorods," *Nanoscale Research Letters*, vol. 9, no. 1, p. 673, 2014.
- [27] M. K. Singh, P. Chettri, A. Tripathi, A. Tiwari, B. Mukherjee, and R. K. Mandal, "Defect mediated magnetic transitions in Fe and Mn doped MoS₂," *Physical Chemistry Chemical Physics*, vol. 20, no. 23, pp. 15817–15823, 2018.
- [28] S. B. Desu and E. C. Subbarao, "Effect of oxidation states of Mn on the phase stability of Mn-doped BaTiO₃," *Ferroelectrics*, vol. 37, no. 1, pp. 665–668, 2011.
- [29] A. K. Singh, J. Prasad, U. P. Azad et al., "Vanadium doped few-layer ultrathin MoS₂ nanosheets on reduced graphene oxide for high-performance hydrogen evolution reaction," *RSC Advances*, vol. 9, no. 39, pp. 22232–22239, 2019.
- [30] J. Zhou, H. Xiao, B. Zhou et al., "Hierarchical MoS₂-rGO Nanosheets with High MoS₂ loading with enhanced electrocatalytic performance," *Applied Surface Science*, vol. 358, pp. 152–158, 2015.
- [31] M. Zhong, C. Shen, L. Huang et al., "Electronic structure and exciton shifts in Sb-doped MoS₂ monolayer," *Materials and Applications*, vol. 3, no. 1, 2019.
- [32] K. Chen, M. Wang, G. Li, Q. He, J. Liu, and F. Li, "Spherical α -MnO₂ supported on N-KB as efficient electrocatalyst for oxygen reduction in Al-air battery," *Materials*, vol. 11, no. 4, p. 601, 2018.
- [33] J. Chen, B. Zhu, Y. Sun et al., "Investigation of low-temperature selective catalytic reduction of NO_x with ammonia

- over Mn-modified $\text{Fe}_2\text{O}_3/\text{AC}$ catalysts,” *Journal of the Brazilian Chemical Society*, vol. 29, pp. 79–87, 2018.
- [34] V. Hiremath, M. Cho, and J. G. Seo, “Self-assembled Mn_3O_4 nano-clusters over carbon nanotube threads with enhanced supercapacitor performance,” *New Journal of Chemistry*, vol. 42, no. 24, pp. 19608–19614, 2018.
- [35] N. Tronganh, Y. Yang, F. Chen et al., “ SiO_2 -assisted synthesis of layered MoS_2 /reduced graphene oxide intercalation composites as high performance anode materials for Li-ion batteries,” *RSC Advances*, vol. 78, 2016.
- [36] S. Li, H. Wang, K. Cao, and P. Huo, “Fabricated Ag dots/flower-like MoS_2 /rGO multidimensional photocatalyst for enhanced photocatalytic activity,” *Journal of the Taiwan Institute of Chemical Engineers*, vol. 104, pp. 177–186, 2019.
- [37] J. Zhang, Y. Xu, Z. Liu, W. Yang, and J. Liu, “A highly conductive porous graphene electrode prepared via in situ reduction of graphene oxide using Cu nanoparticles for the fabrication of high performance supercapacitors,” *RSC Advances*, vol. 5, no. 67, pp. 54275–54282, 2015.
- [38] A. Syari’ati, S. Kumar, A. Zahid et al., “Photoemission spectroscopy study of structural defects in molybdenum disulfide (MoS_2) grown by chemical vapor deposition (CVD),” *Chemical Communications*, vol. 55, no. 70, pp. 10384–10387, 2019.
- [39] F. A. Aisien, N. A. Amenaghawon, and E. F. Ekpenisi, “Photocatalytic decolourisation of industrial wastewater from a soft drink company,” *Journal of Engineering and Applied Sciences*, vol. 9, pp. 11–16, 2013.
- [40] J. Lim, H. Kim, P. J. J. Alvarez, J. Lee, and W. Choi, “Visible light sensitized production of hydroxyl radicals using fullerol as an electron-transfer mediator,” *Environmental Science & Technology*, vol. 50, no. 19, pp. 10545–10553, 2016.
- [41] Z. Cheng, F. Bing, Q. Liu, Z. Zhang, and X. Fang, “Novel Z-scheme visible-light-driven $\text{Ag}_3\text{PO}_4/\text{Ag}/\text{SiC}$ photocatalysts with enhanced photocatalytic activity,” *Journal of Materials Chemistry A*, vol. 1–3, pp. 1–8, 2014.
- [42] L. Shi, L. Liang, J. Ma, F. Wang, and J. Sun, “Enhanced photocatalytic activity over the $\text{Ag}_2\text{O-g-C}_3\text{N}_4$ composite under visible light,” *Catalysis Science & Technology*, vol. 4, no. 3, pp. 758–765, 2014.
- [43] L. Shi, L. Liang, J. Ma, F. Wang, and J. Sun, “Remarkably enhanced photocatalytic activity of ordered mesoporous carbon/g- C_3N_4 composite photocatalysts under visible light,” *Dalton Transactions*, vol. 43, no. 19, pp. 7236–7244, 2014.